Nanocomposite thermoset of tannic acid-based epoxy and iron oxide nanoparticle decorated cellulose nanofibers

Highlights

With the objective of designing a sustainable epoxy system with high performance and multifunctional attributes, this chapter demonstrates the development of a biogenic nanohybrid made up of cellulose nanofibers (CNFs) and innocuous iron oxide nanoparticles (IONPs) and its nanocomposite with a bio-based epoxy. Industrial waste tea fibers (WTFs) were utilized in the previous chapter for the generation of CNFs and now these were further employed for the extraction of tea polyphenols. Aided by this tea polyphenolic extract, iron oxide nanoparticles were produced on the surface of CNFs through an "in situ nucleation and growth" approach. Subsequently, the nanohybrid was incorporated into a bio-derived epoxy (tannic acid epoxy, TAE) to reinforce the latter and to attain better mechanical and thermal properties. Further, considering the unfortunate negligence experienced by epoxy systems in the field of biomedical science and engineering, the nanocomposite was explored as a stimuli-responsive drug vehicle for the delivery of ampicillin. The bactericidal activity of the drug-loaded nanocomposites against multiple bacterial strains corroborated the drug release behavior. The biocompatible and biodegradable nanocomposite provided adequate efficiency to be explored in different realms of biological research.

Parts of this chapter is published in

Borah, N., Rather M. A., Bhar, B., Mandal, B. B., Mandal, M., and Karak, N. A high-performance epoxy nanocomposite with iron oxide decorated cellulose nanofiber as a sustained drug delivery vehicle for an antibacterial drug. *New Journal of Chemistry*, 2023, (***Manuscript accepted***).

5.1. Introduction

In recent times, the preparation of high-performance hybrid materials tailored with different biopolymers and transition metal oxide nanoparticles mineralized on their surfaces has gained great attention [1]. As perceived from the discussion provided in **Chapter Four**, cellulose is one such ubiquitous biopolymer suitable for obtaining promising nanohybrids or composites having pertinency in electronics, semiconductors, absorption, gas sensors, catalysis, etc. [2]. Different nanostructures, such as cellulose nanocrystals, CNFs, etc., have been employed for enhancing the strength and toughness of epoxy, but occasionally lead to compromised performances. Fascinatingly, the integration of nanocellulose with rigid inorganic nanostructures (especially metal oxides such as zinc oxide (ZnO), iron oxide (FeO), titanium oxide (TiO_2), silver oxide (Ag_2O), etc.) has been declared to synergistically improve the thermo-mechanical performance and barrier properties of the hybrids, along with the introduction of other adventitious attributes [2, 3]. For instance, recently Sen et al. described the design of a thermally insulating nanocomposite aerogel from iron oxide nanoparticles (IONPs) grown over CNFs [4]. Breijaert et al. made such an attempt by preparing in-situ self-assembled iron oxide over functionalized nanocellulose [5]. The nanohybrid was then studied for controlled delivery of drugs in the presence of daylight via an adsorption-desorption mechanism [5].

Among the various metal oxide-based nanostructures studied, IONPs are the most innocuous, biocompatible, cost-effective, easily processible nanoparticles, bestowing them with comprehensive pertinency. Mostly, plant- and microbe-mediated biogenic IONPs are in a leading position as conventional chemical reduction or hydrothermal methods are associated with toxicity and energy consumption issues [6]. Tea polyphenols have evolved to be a potential reducing agent and stabilizer for IONPs. Several articles have already been described the success of tea polyphenols in inducing nanoparticle growth at ambient reaction conditions [7]. Furthermore, the waste or residue generated from the polyphenol extraction processes are good sources of cellulose and can be judiciously utilized for deriving nanocellulose.

Implantation of metal-based devices inside the living body is often associated with post-surgical infections that have been proven to be lethal [8]. Applying infection-resistant coatings, which can release antimicrobial particles or drugs loaded in them and simultaneously degrade *in vivo* after completion of their service can provide a prolific

solution to such problems. Epoxy resin, being a dominant candidate in the coating-based industries, has been rarely explored as a drug carrier coating for metallic implants or other metal-based apparatus used in biomedical applications. When it comes to bio-based epoxies, the lack of innovative research can be well realized in such application-oriented biomedical domains, which became the core inspiration of this present study. In a recent study by Zou et al., a hyperbranched epoxy was loaded with curcumin and MXene to prepare bactericidal patches. The study focused on self-healing and shape memory attributes as well as curcumin-induced antibacterial activity of the patches but remained silent on their release profiles [8].

Considering the above discussion, the agenda of this work was to fabricate a bio-epoxy-based, mechanically strong, biocompatible nanocomposite system using an innocuous nanohybrid made up of IONPs grown over CNFs that can be tuned for different propitious applications. Primarily, the IONP@CNF nanohybrid was prepared by a facile and sustainable route by growing IONPs *in situ* over the surface of CNFs at room temperature (RT) in an aerobic environment. Then, the prepared nanohybrid was incorporated into bio-based epoxy TAE in low weight percents (wt%). The presence of the nanohybrid significantly affected the mechanical strength and boosted the thermal performance of the epoxy thermosets. The hemolysis, cell viability, and accelerated biodegradation study explicitly confirmed the biocompatibility and biodegradability of the nanocomposite. Finally, a drug release study was carried out for all the compositions of the nanocomposites and at different pHs for the most suitable nanocomposite. The antibacterial results further affirmed the drug-carrying capability of the nanocomposite system and its efficacy as an infection-resistance system in biomedical research.

5.2. Experimental

5.2.1. Materials

All the chemicals utilized in the preparation of TAE resin and CNFs, inclusive of tannic acid (TA), epichlorohydrin, sodium hydroxide, acetic acid, hydrogen peroxide, etc., were purchased from the same suppliers as described in **Chapters Two**, **Three,** and **Four** with identical specifications.

Ferrous sulfate heptahydrate ($FeSO_4.7H_2O$) is an iron (II) salt with pale blue-greenish crystals. The seven water molecules are coordinated to the iron (II) cation, satisfying its secondary valency. Having the ancient names, “green copperas” or “green

vitriol", $FeSO_4.7H_2O$ has a molecular weight of 278.02 g/mol and exceptionally good solubility in water. $FeSO_4.7H_2O$ has an octahedral geometry and is paramagnetic in nature. It is used in nutritional supplements, water treatment, agriculture, industries, and medical sciences for different purposes. In this work, it is used as the prime source of iron to prepare IONPs and was supplied by HiMedia in India.

Ampicillin (AC) is a broad-spectrum antibiotic, which falls under the classification of penicillin. AC has a similar structure to penicillin and is active against various infections caused by bacteria. Its mode of action involves weakening the cell walls of bacterial species, which results in rupturing and finally death of the bacteria. In the present investigation, AC was used in the drug release study and was supplied by Merck in India.

Phosphate buffer saline (PBS) tablets used for the drug release study were obtained from HiMedia, India. The total phenolic content of the tea polyphenols was measured using Folin Ciocalteu reagent, which was purchased from SRL, India.

Different microbial cultures employed for the testing of the antibacterial activity of the materials, such as *Escherichia coli* (MTCC 40) (*EC*), *Staphylococcus aureus* (MTCC 3160) (*SA*), *Bacillus cereus* (MTCC 430) (*BC*), *Klebsiella pneumonia* (MTCC 618) (*KP*), *Pseudomonas aeruginosa* (MTCC 2297) (*PA*), *Basilus subtilis* (MTCC 121) (*BS*), and *Yersinia enterocolitica* (MTCC 859) (*YE*) were purchased from the Microbial Type Culture Collection and Gene Bank (MTCC) Chandigarh, India, while *Salmonella typhimurium* (ATCC 14038) (*ST*) was purchased from the American Type Culture Collection (ATCC). The cultures were revived and stored at -80 ℃ in 20% glycerol stock. Luria Bertani (LB) and Tripton Soy Broth (TSB) used as nutrient medium for the growth of the above-stated bacterial species were purchased from HiMedia, India.

5.2.2. Instrumentation

The nanostructure and morphology of the prepared nanohybrid IONP@CNF and nanocomposites were identified using a field emission scanning electron microscope (FESEM, Model JOEL, Japan). The chemical structure and bonding interactions present in CNFs and IONP@CNFs were studied using an X-ray photoelectron spectrometer (XPS, Model ESCALAB Xi+, Thermo Fisher Scientific Pvt ltd, UK). Other instrumentations such as FTIR, XRD, SEM, TEM, TGA, DSC, etc. used for the scrutinization of the nanomaterials and nanocomposites were the same as mentioned in **Chapters Two** and **Four**.

Different mechanical performances of the nanocomposites were investigated using UTM, impact, and scratch resistance testers, as detailed in **Chapter Two** under **Section 2.2.2**. The tests were performed consecutively for more than three samples, and their average results were reported.

5.2.3. Methods

5.2.3.1. Preparation of tea extract (TE)

The WTFs were carefully washed with distilled water for removing impurities and then air-dried. About 2 g of these fibers were placed in 100 mL of deionized (DI) water and performed magnetic stirring for 30 minutes (min) at 50 ℃. Upon cooling to RT, the content was sequentially filtered with a normal and then with a Whatman filter paper. The final step was centrifuging the filtrate and storing the supernatant extract (TE) at 4 ℃ for future applications. The residue left during filtration was then dried in an oven at 60 ℃ for further usage in deriving CNFs.

5.2.3.2. Extraction of CNFs from WTFs

CNFs were obtained from the residual WTFs by successive mechano-chemical treatments as described in **Section 4.2.3.1** of **Chapter Four.**

5.2.3.3. Preparation of the IONP@CNF nanohybrid

The IONPs supported over CNFs were prepared by the coprecipitation method using TE as the reducing agent. Initially, 30 mL of a 0.1 M $FeSO_4.7H_2O$ solution was taken in a round-bottom flask with magnetic stirring. To the above solution, 30 mL of CNF dispersion (2.5 mg/mL) was added and left for overnight stirring at RT. It was followed by the addition of 15 mL of TE to the mixture dropwise with the aid of a dropping funnel when the color of the solution (which was initially pale yellow) started changing to black. After completion of the addition, the pH of the solution was increased to 8 by adding a few drops of 0.5 M NaOH solution. The black product obtained was successively washed with DI water via centrifugation to neutralize the pH and freeze-dried to get the IONP@CNF nanohybrid. For further use, the nanohybrid was also dispersed in tetrahydrofuran (THF) and stored.

5.2.3.4. Fabrication of the epoxy nanocomposite

The IONP@CNF/TAE nanocomposite was fabricated following a solvent-assisted mixing technique. At first, the bio-based epoxy TAE was synthesized from TA and

epichlorohydrin following the procedure explained in **Chapter Two**, **Section 2.3.2.1**. This TAE was further used as the matrix for the preparation of the nanocomposite. Especially, for 3 g of TAE, different weight percent (wt%) of IONP@CNF nanohybrid suspension was added followed by the addition of 1-2 mL of distilled THF. The mixer was then subject to ultrasonication for 20 min in a 3 mm probe sonicator at 0.5 cycles per second at 60% amplitude. The content was then mechanically blended at 80 ℃ for 30 min till the solvent completely evaporated and a homogeneous nanocomposite mixture was attained. On cooling, the nanocomposite was mixed with a proper amount of hardener and cast on glass plates, followed by the degassing of residual solvent in a vacuum system. The films that became touch-free were cured at 100 ℃ and post-cured at 120 ℃ for the specified period of time. By adjusting the weight ratio of IONP@CNF to TAE at 0.25, 0.5, and 1.0, three different compositions of the nanocomposites were prepared and codified as IO@CNF0.25/TAE, IO@CNF0.50/TAE, and IO@CNF1.00/TAE, respectively.

5.2.3.5. Determination of total phenolic content

The presence of total phenolic content in the tea extract was determined using the Folin-Ciocalteu reagent by following the Singleton procedure [9]. Initially, to 0.3 mL of diluted TE, 2.7 mL of ten times diluted Folin-Ciocalteu reagent was added and mixed properly. To this solution, 2 mL of 7.5% sodium carbonate solution was added, followed by incubating the mixture for 15 min in the dark. Afterward the absorbance of the sample was recorded at 760 nm using a UV-visible spectrophotometer. The standard curve was plotted using five known concentrations of gallic acid (from 40 mg/L to 200 mg/L), and from this curve, the total phenolic content of TE was evaluated in mg gallic acid equivalent (GAE) per g of WTF.

5.2.3.6. Hemolytic activity study

The method described by Rather et al. was followed to investigate the hemolytic activity of IO@CNF1.00/TAE nanocomposite at different concentrations (1 mg, 5 mg, and 10 mg, in duplicates) [10]. Firstly, 40 mL of defibrinated sheep blood (ThermoFisher Scientific) was centrifuged at 10,000 rounds per min (rpm) for 15 min at 4 °C. The supernatant was discarded, and the pellet was washed with 0.9% NaCl solution and centrifuged again at 10,000 rpm for 15 min at 4°C. The washing was repeated two times, and the final pellet was suspended in 0.9% NaCl. The red blood cell (RBC) suspension was pipetted into different centrifuge tubes. Finally, samples were added to centrifuge tubes to make the

final concentrations of 50, 100, 150, and 200 µg/mL. The reaction mixture was placed at 37°C for 30 min and centrifuged at 10,000 rpm for 5 min. Then, 200 µL supernatant from each centrifuge tube was poured into a 96-well plate, and the optical density (OD) was measured at 540 nm (Thermo Scientific Multiscan GO) to quantify cell lysis and the release of hemoglobin. Triton-X and water were used as positive controls (PC), while the centrifuge tube with RBC suspension in 0.9% NaCl served as a negative control (NC). The percent of hemolysis was calculated as follows.

$$\text{Hemolysis (\%)} = [(AB_S - AB_{NC})/ (AB_{PC}\text{-}AB_{NC})] \times 100 \qquad \textbf{Equation 5.1}$$

where AB_{PC} is the absorbance of the positive control, AB_{NC} is the absorbance of the negative control, and AB_S is the absorbance of the treated samples.

5.2.3.7 *In vitro* biocompatibility assessment

Biocompatibility assessment of the fabricated nanocomposites and TAE thermosets was conducted using human dermal fibroblasts (HDF) via the live-dead assay. The cells were procured from Himedia, India, and cultured in high glucose DMEM (Gibco; Thermo Fisher Scientific, USA) containing 10% fetal bovine serum (FBS, Gibco; Thermo Fisher Scientific, USA) and 1X antibiotic-antimycotic solution (Himedia, India). The films (5×5 mm^2) were sterilized using (70% v/v) for 10 min, rinsed with PBS, and preconditioned in media for 24 hours (h). HDF cells were trypsinized when they reached 70-80% confluence and seeded (~$2x10^4$ cells on each) on the films and tissue culture plate (TCP). TCP was considered as the control surface for comparison. The seeded cells were assessed using live-dead (Sigma-Aldrich, USA) reagents on day 1 and day 7 after seeding. At first, the cell-seeded films and TCP were gently washed with PBS and incubated with a solution containing 4 µM calcein–AM (stains adherent live cells and shows green fluorescence) and 2 µM ethidium homodimer (stains dead cells and shows red fluorescence) for 15 min 37 °C in humidified incubator [11]. After staining, the samples were washed with PBS and were imaged using a fluorescent microscope (ZEISS Axio Observer, Germany) and representative images were presented.

5.2.3.8. Ampicillin (AC) loading into the nanocomposite

In order to encapsulate AC into the resinous nanocomposite, the drug was dissolved in 100 µL of distilled water, and to this mixture, the required amount of IONP@CNF dispersion was added with magnetic stirring for 1 h. Then this mixture of drug and IONP@CNF was added to TAE and finally stirred at 70 °C for 30 min to obtain the nanocomposite. The

thermosets were then prepared by mixing them with the hardener and cured at RT for 3 days. The thermosets were then washed with water to remove any loosely adhered AC, and the aliquot was measured for any traces of AC using a UV-visible spectrophotometer at 227 nm wavelength against a standard AC concentration curve. From the amount of AC leached out, the encapsulation efficiency (EE) was calculated using the following equation.

$$EE\ (\%) = [(M_0 - M_r)/M_0] \times 100 \qquad \textbf{Equation 5.2}$$

where M_0 and M_r are the amounts of drug initially added and leached out during washing from the thermoset, respectively.

5.2.3.9 Ampicillin (AC) release and kinetic study

The AC release rates from the nanocomposite thermosets were studied in PBS solution at 37 ℃ for a period of 5-7 days. For each composition, a definite amount of thermoset was cut into small pieces, immersed in 100 mL of PBS solution, and placed in an incubator shaker at a temperature of 37 ℃. Aliquots were taken from the solution at particular time intervals and replaced with fresh PBS solution to maintain a constant volume. The absorbance of these aliquots was measured in a UV-visible spectrophotometer at a 227 nm wavelength, from which the amount of AC released was calculated with the assistance of the standard curve. The process was repeated thrice. In order to calculate the cumulative drug release rate, the following equation was utilized.

$$\text{Cumulative release}\ (\%) = (M_t/M_0) \times 100 \qquad \textbf{Equation 5.3}$$

where M_t is the amount of drug released at a particular time and M_0 is the amount of drug initially loaded, respectively.

Similarly, the kinetics of drug release were studied using four different models, namely, zero order, first order, Korsmeyer-Peppas model, and Higuchi model as shown in **Table 5.1**, **Equations 5.4 – 5.7** [12]. The best-supported model was evaluated using the curve fitting method and the correlation coefficient value corresponding to each model.

5.2.3.10. Antimicrobial activity study

The antimicrobial activity of 10% AC-loaded films against both gram-positive and gram-negative pathogenic bacteria was determined using the agar diffusion method [13].

Bacterial cultures of different bacterial species *(SA, ST, EC, BC, PA, YE,* and *KP)* were grown overnight in LB and TSB. The OD at 600 nm of the fresh cultures was set at 0.4 which was used in the experiment. The cultures (100 μL) were spread on the prepared LB

Table 5.1: Kinetic models with equations utilized for studying the drug release mechanism

Model	Equation	Graph axes	Equation No.
Zero order	$M_t = K_0t + M_e$	Cumulative release vs time	**5.4**
First order	$\log (M_e - M_t) = -(K_1/2.303)t + \log M_e$	Log cumulative release vs time	**5.5**
Korsmeyer - Peppas	$M_t/M_e = K_m(t)^n$	Log cumulative release vs time	**5.6**
Higuchi	$M_t = K_H (t)^{1/2}$	Cumulative release vs $(\text{time})^{1/2}$	**5.7**

where M, K, t, and n referred to amount of drug released at a particular time, rate constant, time, and release exponent, respectively

agar plates. The films were placed onto the agar plates and incubated overnight at 37 ℃ for 24 h. After incubation, the plates were evaluated for antimicrobial activity, and the zone of inhibition (ZOI) was measured accordingly.

The biodegradation test was performed for the nanocomposite without AC and TAE thermosets following the procedures as stated in **Chapter Two, Section 2.2.3.5,** using *BS* as the bacterial strain.

5.3. Results and discussion

5.3.1. Biogenic synthesis of IONP@CNFs

The plant-mediated growth of IONPs is a propitious approach to attain highly innocuous and biocompatible nanoparticles. In this study, TE derived from WTFs has been utilized to synthesize IONPs on the surface of CNFs. Tea is the second most widely used beverage, which is enriched with bioactive compounds such as polyphenols (especially catechins or gallocatechins), flavonoids, alkaloids, amino acids, vitamins, carbohydrates, etc. [14, 15]. Although the detection or estimation of each component is out of the scope of this study, realizing the active role of

polyphenols in the formation of IONPs from the previous literature [7], the total phenolic content was evaluated using the Folin-Ciocalteu method. The total phenolic content of TE was calculated to be 399.2 ± 2.9 mg GAE per gram of tea fibers taken, which unveiled the abundant presence of phenolic compounds in the extract. These polyphenols are supposed to initiate the incidental reduction of Fe^{2+} to black-brown colored IONPs, changing the color of the solution to black-brown due to the surface plasmon resonance (SPR) of IONPs. There are numerous studies available in the literature showing plant extract-mediated synthesis of IONPs [16-18]. IONPs decorated onto cellulose-based templates have also been studied [4, 19]. But most of the time, the synthesis involved harsh or laborious chemical conditions such as strong reducing agents (NaOH, NH_4OH, etc.), high temperatures, an inert (N_2) atmosphere, etc. In this work, the authors have tried to generate IONPs over the surface of CNFs using TE as the green reducing agent at RT under aerobic conditions, which is so far attempted for the first time. **Figure 5.1** shows the representation of the synthesis procedure of IONP@CNFs using TE.

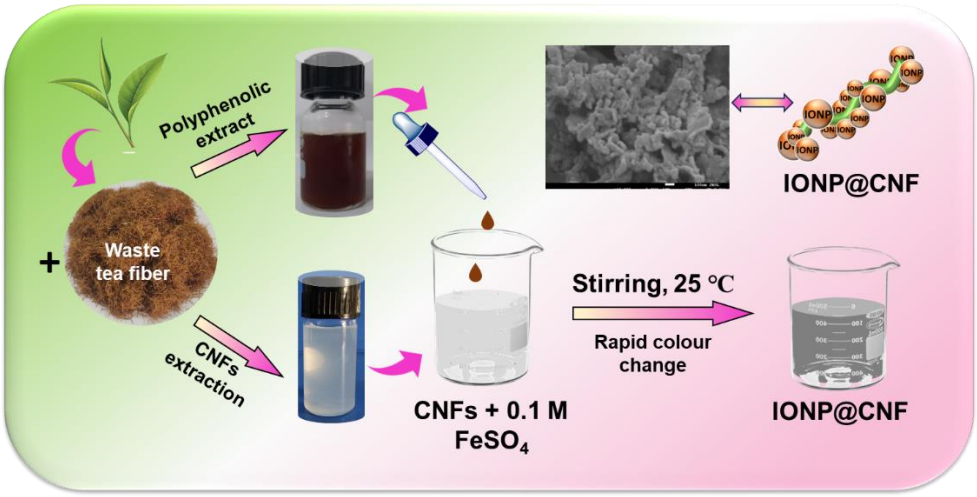

Figure 5.1: Scheme showing TE assisted in-situ growth of IONPs over CNFs

5.3.2. Characterization of the nanohybrid

The successful formation of the IONPs was initially confirmed by recording the UV-visible spectra of the Fe^{2+} precursor, IONP@CNF and bare IONP suspensions in water. As evident from the literature, depending on the precursor and the reducing agent used, the peak corresponding to IONPs in the UV-visible spectra varies from 200-400 nm wavelength range [18]. To authenticate the same, bare IONPs were synthesized using the same procedure, the only difference being that the CNFs were not used as the support for growing the nanoparticles. **Figure 5.2(a)** shows the UV-

visible spectra of Fe^{2+} salt solution, bare IONPs, and IONP@CNFs nanohybrid. The peak appearing at 250 nm wavelength in the precursor shifts to 270 nm when nanoparticles are formed simultaneously in bare IONPs and the nanohybrid. The FTIR spectra of CNFs and IONP@CNFs were recorded along with bare IONPs and are presented in **Figure 5.2(b)**. It can be seen from the figure (spectrum (i)) that the characteristic peaks of CNFs appear at 3400 cm^{-1} corresponding to -O-H stretching vibration, at 2900-2800 cm^{-1} for -C-H stretching vibrations, and at 1645 cm^{-1} for -O-H bending vibration of absorbed water in CNFs [20, 21]. Similarly, peaks at 1443 cm^{-1}, 1322 cm^{-1}, and 1047 cm^{-1} were ascribed to the -C-O-H stretching, $-CH_2$ wagging, and -C-O-C- stretching vibrations of the pyranose ring, respectively, and also appeared in the spectrum of CNFs [20]. All these peaks were detected in the spectrum of IONP@CNFs nanohybrid (spectrum (ii) in **Figure 5.2(b)**) as well. However, the characteristic peak for the Fe-O bond that normally appears at around 630-550 cm^{-1} was absent due to overlapping with other bands [19, 20]. On recording the FTIR spectrum of the bare IONPs (spectrum (iii)), a small peak appeared at 618 cm^{-1} that corresponded to Fe-O stretching. On further treatment at a high temperature (250 ℃ for 3 h) of the IONPs, this peak appeared more intense, as evinced from the spectrum (iv) of **Figure 5.2(b)**. Similar results were also recorded by Kargar et al. [22] and Sen et al. [4].

The crystal structure of the IONP@CNFs was investigated by recording their XRD patterns and a comparison with that of CNFs was performed as presented in **Figure 5.2(c)**. The conventional crystalline peaks of CNFs appeared at 22° and 15° for the corresponding planes (200) and (110). However, owing to the presence of tea polyphenols over the surface of IONPs, the XRD peaks for conventional IONPs were absent in the Xray diffractogram of IONP@CNFs. This revealed the highly amorphous character of the nanoparticles. Previously synthesized IONPs (Fe_2O_3) that were exclusively derived from TE, unveiled similar results, as stated by Plachtová et al. [7]. A critical investigation of the spectrum for IONP@CNFs revealed that the crystalline peak of the (200) plane that originates from CNFs disappeared here, indicating a significant loss of crystallinity in the nanohybrid. However, some small peaks appeared at 26°, 36°, 41°, and 47° indicating the phase structure of the nanoparticles to be similar to Fe_2O_3 [18]. Maghemite (γ-Fe_2O_3) and magnetite (Fe_3O_4) have nearly similar XRD patterns, for which they become indistinguishable. But the appearance of a peak in maghemite at $23° < 2\theta < 27°$ (which

also appeared in the nanohybrid at 26°) can be considered for distinguishing maghemite from the latter [23].

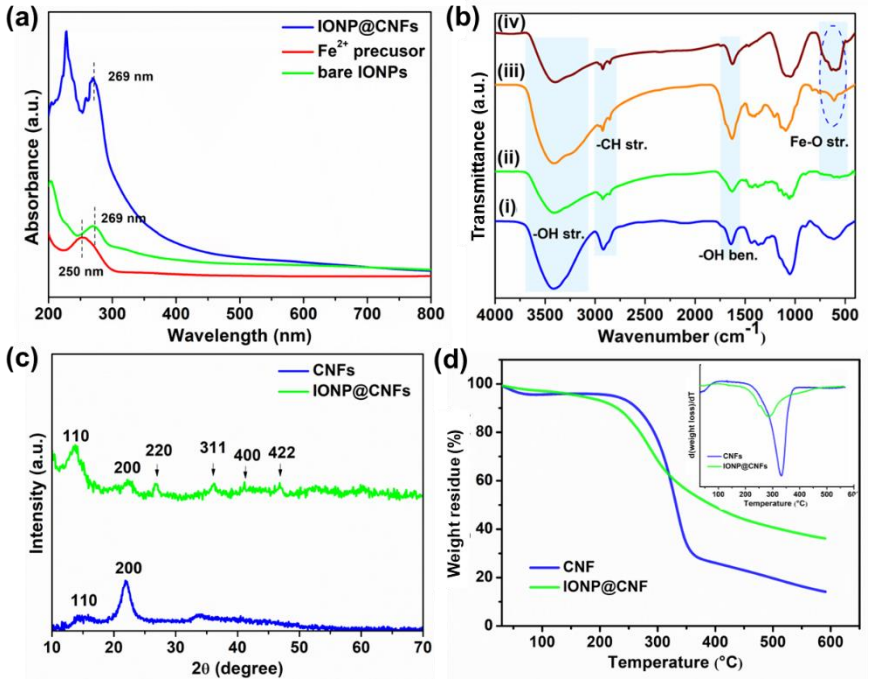

Figure 5.2: (a) UV-visible spectra of bare IONPs, Fe^{2+} precursor and IONP@CNFs nanohybrid; (b) FTIR spectra of (i) CNFs, (ii) IONP@CNFs nanohybrid, (iii) bare IONPs, and (iv) IONPs after annealing; (c) powder XRD patterns of CNFs and IONP@CNFs; thermal stability analysis as (d) TGA and DTG (inset) profiles

For assessing the thermal stability of the nanohybrid, thermogravimetric analysis was performed, and the TGA thermograms of CNFs and IONP@CNFs are presented in **Figure 5.2(d)** with inset DTG curves. The initial weight loss of 4.5% observed in CNFs around 100 ℃ can be referred to as the evaporation of absorbed water, which was followed by a plateau that continued to 230 ℃ with a residual weight of 95%. The prime degradation started after this temperature as the cellulose started to depolymerize at this point, and a sharp drop was seen in the thermogram with the peak degradation temperature at 330 ℃. The degradation continued till 380 ℃ and after this stage, the degradation slowed down until the final temperature of 600 ℃ was attained with a weight residue of 14.4%. Generally, as the literature suggests, the incorporation of IONPs increases the thermal stability of cellulose by shifting the degradation to higher temperatures [4]. But, in the case of IONP@CNFs, the opposite trend was noticed in **Figure 5.2(d)** as the degradation of IONP@CNFs started at a slightly lower temperature (204 ℃) than CNFs, followed by the usual degradation of the cellulose structure. The presence of different bioactive compounds complexing with the IONPs over the surface of the

CNFs was found to be responsible for such earlier degradation [24]. This kind of behavior has already been noticed in some other plant extract-derived IONPs [25]. The IONPs synthesized by Baghdadi et al. revealed similar results, with an earlier thermal degradation pattern recorded for organically modified IONPs compared to pure IONPs [26]. However, the residual weight after complete degradation was found to be 36% which is 2.5 times greater than that of CNFs, indicating the presence of a sufficient amount of iron in the nanohybrid.

In order to further validate the chemical linkages and investigate the surface electron structures of the nanohybrid, XPS spectra of CNFs and IONP@CNFs were recorded. **Figure 5.3(a)** shows the survey spectra where the presence of major elements C 1s, O 1s in CNFs and C 1s, O 1s, Fe 2p in IONP@CNFs can be detected. On deconvoluting the C 1s spectrum of CNFs, three distinct peaks appeared, as seen in **Figure 5.3(b)** for the C 1s of CNFs. They can be respectively assigned for the C-C/C-H bond at 284.5 eV, C-O bond at 286.3 eV, and the C-O-C bond at 287.8 eV.

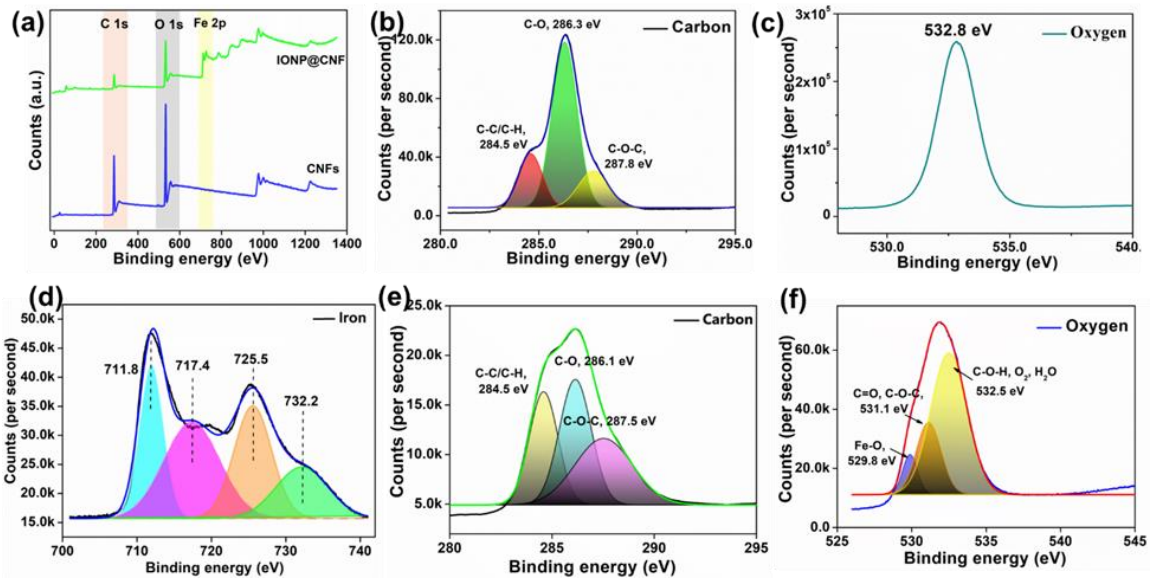

Figure 5.3: (a) Comparison of XPS survey spectra of CNFs and IONP@CNFs; deconvoluted single spectrum of (b) carbon and (c) oxygen present in CNFs and (d) iron, (e) carbon, and (f) oxygen present in IONP@CNFs

The O 1s peak appeared at 532.8 eV corresponding to the C-O bond (**Figure 5.3(c)**) [27]. Interestingly, these peaks were also present in the C 1s spectra of IONP@CNFs with slight changes in their positions and intensity, as apparent from the C 1s spectrum in **Figure 5.3(e)**. While the O 1s spectra in **Figure 5.3(f)** of IONP@CNFs detected a peak at 531 eV which can be ascertained to the O-Fe, O-C, and O-H bonds present in the Fe_2O_3, CNFs, and the components of TE. The

narrow-scan spectra recorded for the Fe 2p electrons is shown in **Figure 5.3(d)** with two photoelectron lines at 711.8 eV and 725.3 eV that are the signature peaks for Fe 2p (3/2) and Fe 2p (1/2). A binding energy difference of 13.5 eV was observed between these peaks which is a characteristic of Fe^{3+} species present in Fe_2O_3 [28]. Further confirmation of the presence of Fe^{3+} was obtained from the appearance of two satellite peaks at 719 eV (8 eV higher than the Fe 2p (3/2) peak) and 732 eV. As per the literature, these satellite peaks do not appear or appear with very low intensity in Fe_3O_4 where both Fe^{2+} and Fe^{3+} are present [29]. While species having Fe^{2+} are separated from the main peak by a binding energy of 6 eV only [29]. The results obtained completely coincide with the IONPs prepared by Kasote et al. that were confirmed originally to be Fe_2O_3 [30].

5.3.3. Morphology study of the nanohybrid

The morphological investigation of CNFs and IONP@CNFs performed using SEM, FESEM, and TEM analyses unveiled interesting results. From the SEM images of CNFs presented in **Figure 5.4(a)**, one can observe the smooth surfaces of the nanofibers with a diameter of around 200 nm. When these fibers were coated with IONPs, their surface smoothness decreased significantly. Instead, the fibers were surrounded by amorphous IONPs, and their surfaces appeared rough (**Figure 5.4(b)**). For better transparency, the FESEM images of the freeze-dried

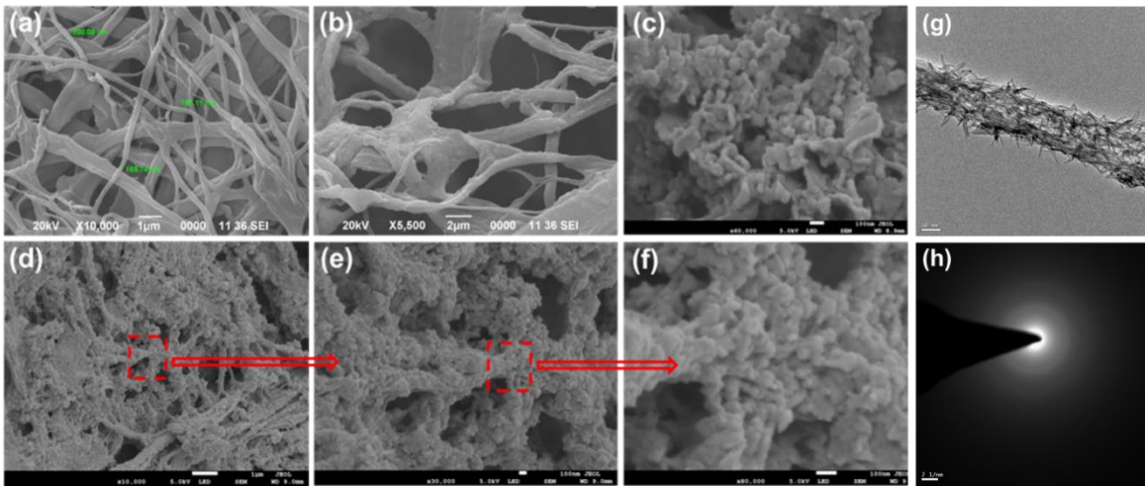

Figure 5.4: SEM images of (a) CNFs and (b) IONP@CNFs; FESEM images at (c) 60,000X, (d)10,000X, (e) 30,000X, and (f) 80,000X magnifications with red rectangular regions being magnified, (g) TEM images of a single strand of IONP decorated nanofiber and (h) SAED pattern of the IONPs decorated nanofiber

IONP@CNFs were recorded as presented in **Figure 5.4(c)-(f)**. The presence of nearly spherical particles over the surfaces, with some inevitable agglomeration, appeared in the FESEM images of IONP@CNFs. The images recorded at four different magnifications (60,000X, 10,000X, 30,000X, and 80,000X respectively, shown in **Figure 5.4(c)**, **(d)**, **(e)**, and **(f)**), respectively illustrate the presence of spherical nanoparticles over the surface of the nanofibers. The average diameter of these nanoparticles as evaluated using the ImageJ software appeared to be 45 nm, with particle sizes ranging from 20 nm to 70 nm. Interestingly, the γ-Fe_2O_3 nanoparticles prepared by Bhosale et al. have analogous morphology, as revealed by the FE-SEM images [31]. To add more, the TEM image of IONP@CNFS in **Figure 5.4(g)** depicts similar results where a single strand of nanofiber can be seen wrapped up with spherical IONPs capped by polyphenols. The SEAD pattern recorded for IONP@CNFs further revealed the amorphous nature (**Figure 5.4(h)**) of the nanohybrid, as no discrete crystallinity was observed in it. The EDX spectrum of IONP@CNFs as displayed in **Figure 5.5(b)** revealed the presence of iron on the IONP@CNF surfaces, which was initially absent in CNFs (**Figure 5.5(a)**). The elemental mapping images for carbon, oxygen, and iron are shown in **Figure 5.5(c)**, **(d)**, and **(e)**, respectively, illustrate similar inferences.

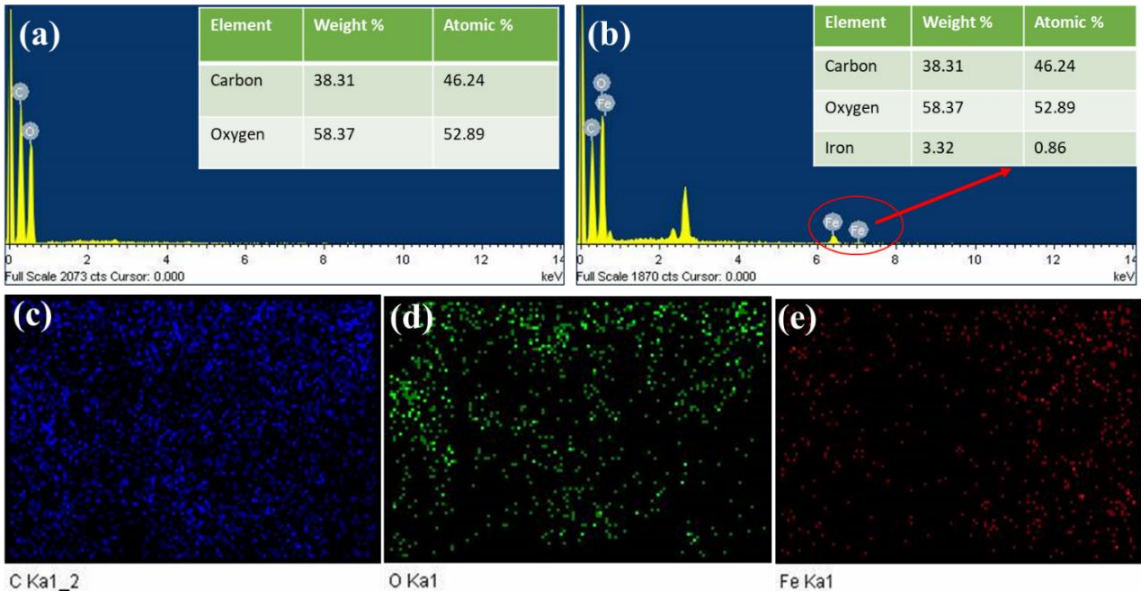

Figure 5.5: EDX spectrum of (a) CNFs and (b) IONP@CNFs with inset atomic wt%, and elemental mapping images for (c) carbon, (d) oxygen, and (e) iron present in IONP@CNFs

5.3.4. Fabrication and characterization of the nanocomposites

Organic coatings, specifically epoxy-based ones with inherent biocompatibility, biodegradability, and infection resistance attributes, are becoming increasingly

important in the field of biomedical sciences. After the detection of the toxicity issues associated with commercially available DGEBA epoxy that originate from the leaching of BPA, the urge for a non-toxic and biocompatible epoxy system with an in-born or adventitious germicidal attribute and UV blocking ability has elevated in recent times. To address the matter, the prepared IONP@CNF nanohybrid was incorporated into the TAE system. The resultant nanocomposite exhibited improved thermal and mechanical properties. Moreover, good transparency, and superior UV blocking properties, as well as sustained drug release profiles are additionally achieved for the nanocomposites. Considering our knowledge in the field, this is the first report on an epoxy system that has been explored as a drug release vehicle.

Figure 5.6(a) shows the ATR-FTIR spectra of all the nanocomposites along with pristine TAE. As apparent from the figure, the nanocomposites possessed all the characteristic peaks that are present in TAE thermoset. The broad band around 3300 cm^{-1} is responsible for -OH stretching, and peaks at 2922 cm^{-1} and 2862 cm^{-1} for -CH_2 stretching, a peak 1710 cm^{-1} for the carbonyl group of esters, a peak of 1640 cm^{-1} for amide stretching could be visibly detected. According to Xu et al., the presence of the TA moiety generated some characteristic peaks at 1400-1000 cm^{-1} for carbohydrate or alcoholic C-O-C or C-O bonds [32]. The peak at 867 cm^{-1} corresponded to aromatic C-H deformation, while the original epoxy peaks that appear near 830-900 cm^{-1} could not be detected in the spectra. In powder XRD patterns recorded for the nanocomposites and pristine TAE as displayed in **Figure 5.6(b)**, broad amorphous peaks at a 2θ value of 20° were observed. The absence of the characteristic peaks of the nanohybrid indicated optimum interaction between the matrix and the nanohybrid.

Long-term UV exposure of biomedical appliances for sterilization against microorganisms is often practiced in the medical field. Such long exposure of materials to UV radiation frequently leads to the degradation of chemical bonds, thereby accelerating the early aging of the materials and shortening their service life [19]. Therefore, it is necessary for the prepared nanocomposite to withstand long-term UV light irradiation in order to be explored as an effective UV resistance coating. It has already been proven that epoxy resins have excellent UV absorption abilities for a certain range of wavelengths [19]. Conversely, IONPs have high UV attenuation abilities that make them effective shields against UV light [33]. To

highlight the same, Cardilo et al. have fabricated a sunscreen formulation by encapsulating Fe_2O_3 nanoparticles in poly(lactic acid) microspheres that displayed better sun protection ability than commercial ZnO-based formulations [33]. The nanocomposites prepared here also exhibited good UV blocking ability, as evident from the transmittance percentages of the thermosets (**Figure 5.6(c)**). When the overall transmittance for the range 200-800 nm was considered, the pristine epoxy possessed better transparency than the nanocomposites in the visible region. The reason for the same might be ascribed to the presence of interacting nanomaterials that have blocked the passage of light to some extent.

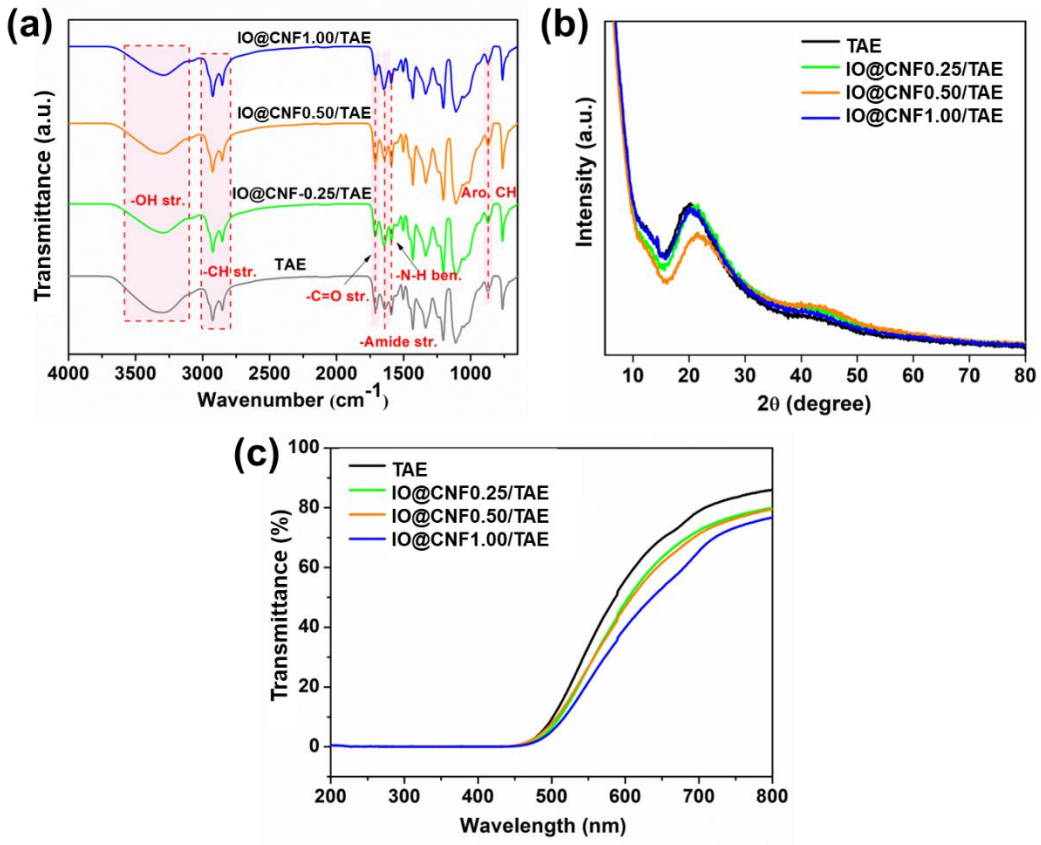

Figure 5.6: (a) ATR-FTIR spectra, (b) XRD diffractograms, and (c) transmittance spectra of the nanocomposite and TAE thermosets

5.3.5. Thermal properties

The thermal stabilities of the nanocomposite thermosets and the pristine epoxy were evaluated using thermogravimetric analysis. **Figure 5.7(a)-(b)** represents the TGA as well as DTG profiles of the thermosets along with IONP@CNFs for comparison purposes. As apparent from the TGA curves, the nanohybrid suffered rapid degradation (the reason for which has been discussed earlier), which was perturbed to some extent when it was incorporated into the epoxy matrix. The thermal

parameters obtained from the study are tabulated in **Table 5.2**. Evidently, the T_{ON} of IONP@CNFs was 204 °C, while the epoxy thermoset has a T_{ON} of around 260 °C as observed from the figure. From these observations, it can be hypothesized that the decomposition profiles of the nanocomposites would appear between those of IONP@CNFs and TAE. The same was reflected in the results. Further, the thermal stabilities of the nanocomposites did not significantly deviate from the pristine after the inclusion of the nanohybrid. Furthermore, the very low nanohybrid content (only 0.25, 0.5, and 1.0 wt%) was insufficient to induce noticeable changes in the thermal stabilities of the nanocomposites, which introduced a positive insight. A similar kind of correlation was noticed in bacterial cellulose and bio-epoxy-containing nanocomposites, where the degradation curves of the nanocomposites were found between those of bacterial cellulose and epoxy [34]. A two-stage degradation was noticed for the thermosets in this instance, however, can be ascribed to the degradation of the chemical linkages originally present in the materials. The first degradation appeared from the depolymerization of TA as well as the damage to ester linkages. The next degradation stage corresponded to the breaking of aromatic rings and the impairment of the cellulose structure [21]. Epoxy nanocomposites derived from DGEBA and functionalized IONPs appeared to exhibit lower thermal stability than neat epoxy [26]. The onset degradation temperatures (which they referred to as T_d) slightly decreased compared to the pristine system when the bare or modified IONPs were introduced in the epoxy. The phenomenon has been reinforced by the fact that the presence of nanoparticles increased thermal transport in the nanocomposites that subsequently resulted in accelerated thermal decomposition [26].

Furthermore, DSC is another essential and systematic method that investigates glass transition temperature (T_g) of a material by measuring the changes in heat flow during successive heating and cooling cycles to identify the transition temperatures [26]. The DSC curves of the nanocomposite thermosets were compared with that of the pristine thermosets and presented in **Figure 5.7(c)**. A clear shift in the deflection points in the curves (marked by red rectangles in the figure) from the pristine system to the highest nanohybrid-containing composition can be detected that indicates positive changes in the T_g values. As apparent from **Table 5.2**, the pristine epoxy has a T_g of 54 °C which increased up to 72 °C in IO@CNF1.00/TAE. Several reports on epoxy nanocomposite show similar results,

revealing enhancements in T_g values with increasing nanomaterial content [35]. The T_g value generally, represents the chain mobility of the polymer matrix in a nanocomposite, which, upon suffering hindrance, shifts to a higher temperature. A number of factors, such as nanosized reinforcing agents, the nature of chemical

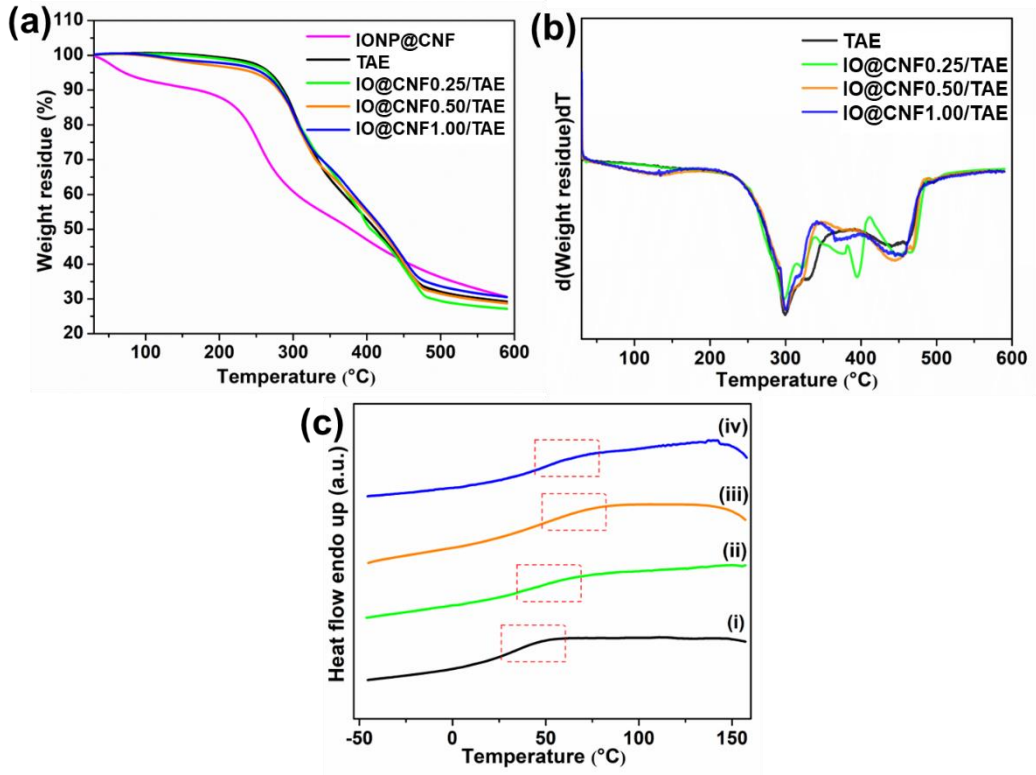

Figure 5.7: Thermal characteristics of the nanocomposites and TAE thermosets displayed in (a) TGA thermograms, (b) DTG profiles, and (c) DSC thermograms of (i) TAE, (ii) IO@CNF0.25/TAE, (iii) IO@CNF0.25/TAE, and (iv) IO@CNF1.00/TAE

functionality, the flexibility of the matrix, etc., strongly alter the transition temperature of a material [35]. As far as the fabricated material is concerned, the presence of the nanohybrid dispersed all over the epoxy matrix might have restricted the movement of the polymer chains via mechanical interlocking, which resulted in a slight increase in the T_g value.

5.3.6. Mechanical properties

Table 5.3 displays the average tensile strengths recorded for the different thermosets (along with standard deviations), and the best profiles are shown in **Figure 5.8**. The incorporation of the nanohybrid positively affected the tensile strength of the nanocomposites and visible enhancements were noticed. The pristine epoxy possessed a tensile strength of 16.73 ± 0.61 MPa. However, the strength

increased from 18.36 ± 0.85 MPa to 23.65 ± 0.77 MPa as the nanohybrid content increased from 0.25 wt% to 0.50 wt% in the epoxy matrix. On further increasing the nanohybrid content to 1.00 wt%, the tensile strength dropped to 21.07 ± 0.46 MPa in IO@CNF1.00/TAE suggesting a possible agglomeration of the nanohybrid

Table 5.2: Different parameters obtained from the thermal study of nanocomposite and TAE thermosets

Parameters	CNF	IONP @CNF	TAE	IO@CNF 0.25/TAE	IO@CNF 0.50/TAE	IO@CNF 1.00/TAE
T_{ON} (°C)	240	209	247	242	241	241
1st stage peak degradation temperature (°C)	331	284	299	300	299	300
2nd stage peak degradation temperature (°C)	-	-	440	450	445	455
Weight residue at 600 °C (%)	14.1	30.7	29.5	27.1	28.8	30.6
T_g (°C)	-	-	54	64	66	72

instead of an even dispersion throughout the matrix [26]. A similar kind of result is reported in the literature, where ZnO/glass fiber-reinforced epoxy exhibited improvement in tensile strengths up to an optimum ZnO content only, after which a similar drop in strength was noticed [36]. The reason for such a trend was referred to as the agglomeration of ZnO nanoparticles [36]. Meanwhile, careful observation of the strain at break values unveiled the effect of the presence of CNFs in the nanocomposites on their flexibility. The elongation values of the nanocomposites were better compared to the pristine, and as per the convection, the values dropped as the tensile strength decreased from IO@CNF0.25/TAE (36.60 ± 2.10%) to IO@CNF1.00/TAE (34.38 ± 1.27%) to IO@CNF0.50/TAE (24.80 ± 0.58%) as their strength increased in the same trend.

The impact strength and scratch hardness values of the nanocomposites are presented in **Table 5.3**. Impact strength values were found to increase upon adding

more and more nanohybrid to the epoxy. In the case of fiber-reinforced epoxy systems, the impact strength greatly depends on the interfacial shear strength between the fibers and the matrix. For better impact resistance, the sudden force applied needs to be dissipated properly from the matrix to the fibers

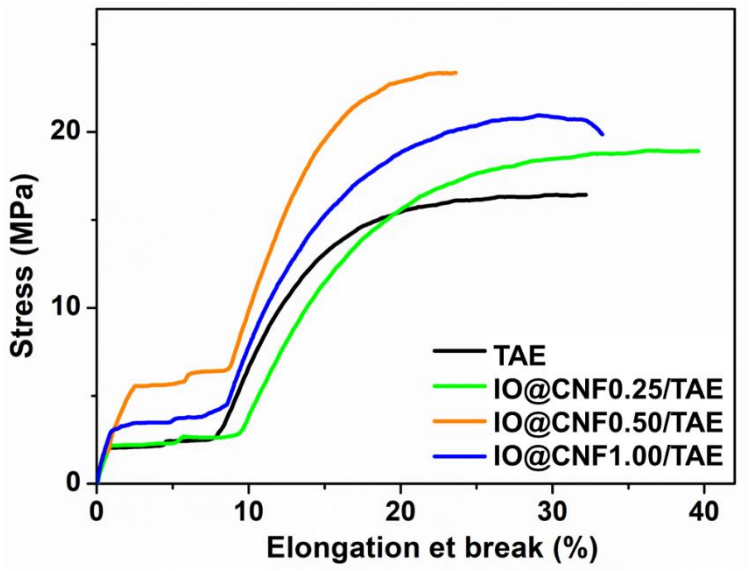

Figure 5.8: Stress-elongation at break profiles of the nanocomposites and pristine TAE thermosets

[36]. The flexibility of the material also plays a crucial role in crack propagation. The simultaneous action of all these factors resulted in an augmentation of impact strength in the nanocomposite system as the nanohybrid content increased. The scratch hardness values also conferred similar facts.

Table 5.3: Mechanical properties of the nanocomposite and TAE thermosets

Sample	Tensile strength (MPa)	Elongation at break (%)	Toughness (J/m^3)	Impact strength (kJ/m)	Scratch hardness (kg)
TAE	16.73 ± 0.61	33.30 ± 1.92	299.1 ± 20.3	16.9 ± 1.2	8.0 ± 0.5
IO@CNF 0.25/TAE	18.36 ± 0.85	36.60 ± 2.10	438.0 ± 34.8	20.1 ± 1.4	8.0 ± 0.5
IO@CNF 0.50/TAE	23.65 ± 0.77	24.80 ± 0.58	315.6 ± 9.0	22.7 ± 2.7	8.5 ± 0.5
IO@CNF 1.00/TAE	21.07 ± 0.46	34.38 ± 1.27	449.8 ± 51.7	25.3 ± 3.1	8.5 ± 0.5

5.3.7. Ampicillin encapsulation and release study

Considering the high crosslinking density of epoxy resins, penetration and diffusion of solvent medium inside the polymer network are cumbersome and their swelling ability is also significantly low. These factors positively affect the EE of the nanocomposites, as a very high EE was obtained for them. The EE was found to be 96%, 92%, and 98% for 10 wt% AC loading, respectively, in IO@CNF0.25/TAE, IO@CNF0.50/TAE, and IO@CNF1.00/TAE. On the other hand, the above-mentioned factors critically affect the drug release profiles as well; the solvent medium cannot effectively enter and carry away the drug with it, leading to low drug release efficiencies. This might be the reason for the scarcity of resources available in the literature on the drug release behaviors of epoxies. Recently, Zou et al. fabricated an antibacterial patch derived from hyperbranched epoxy that was loaded with curcumin [8]. They analyzed the antibacterial properties of the patch along with other parameters but remained silent on the curcumin release profiles of the patches [8]. Considering these facts, the AC-loaded nanocomposites have been cured at RT so as to achieve moderate crosslinking and allow permeation of solvent media through the material.

Howsoever, the release study of AC was performed in PBS media for a period of 5-7 days, and a sustained release profile was recorded for the nanocomposites as shown in **Figure 5.9(a)**. For loading of 10 wt% AC, the release profiles showed a visible relationship with the type of material or the nanohybrid content. Interestingly, all the nanocomposites displayed greater cumulative AC release compared to the pristine (maximum release of 49.7%). The maximum release of 76.6% was recorded for IO@CNF1.00/TAE with an initial burst release that continued for 9 h. This rapid or burst release phase might have appeared because of the dissolution of the AC molecules attached to the surface of the thermosets. However, the release profile sustained up to 7 days for IO@CNF1.00/TAE indicating the capability of the material to withstand a long period and consistently release the drug into the medium. Surprisingly, the nanocomposite with 0.50 wt% nanohybrid content revealed the lowest cumulative release, 59% that sustained up to 6 days, while that with 0.25 wt% loading showed a maximum release of 65%. Evidently, the nanohybrid content present in the polymer affected the release behavior. Here, a clear dependence of the release rate

on the nanohybrid content and crosslinking density can be observed.

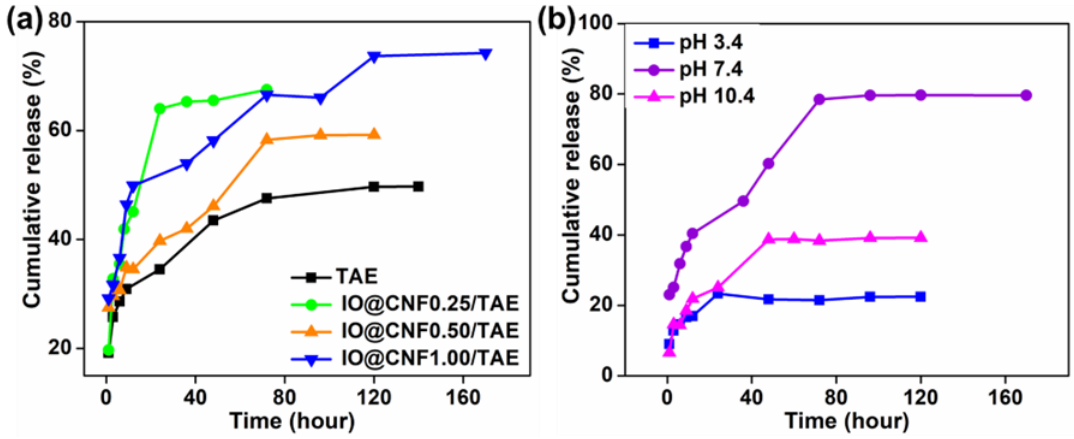

Figure 5.9: AC release profiles of (a) the nanocomposites and TAE in PBS at pH 7.4 and (b) release profiles of IO@CNF1.00/TAE at three different pHs (3.4, 7.4, and 10.4)

5.3.7.1. Effect of pH on ampicillin release

For analyzing the changes in the release rates of AC at different pH environments, a drug release study was performed at three different pHs; 3.4, 7.4, and 10.4 considering IO@CNF1.00/TAE as the release system. As displayed in **Figure 5.9(b)**, the AC release rates were showing pH-responsive behavior. Evidently, the best result was obtained at pH 7.4 with a maximum release of 76.6%, whereas at acidic or alkaline media the release rates declined significantly to 22.4% and 39.1%, respectively. These results demonstrated the pH-responsive release properties of the nanocomposite. As the literature suggests, epoxy systems generally undergo an increment in crosslinking density when subject to acidic or alkaline media [37]. Such effects stem from the presence of H^+, Na^+, Cl^-, OH^-, etc. ions that augment the interaction between the polymer networks [37]. These phenomena affected the diffusion of drug molecules and rendered their movement out of the polymer system, which resulted in low release profiles in acidic or alkaline media.

5.3.7.2. Kinetic study

Drug release is specifically driven by the diffusion of the solvent into the matrix and the dissolution of the drug molecules out of the polymer network. The four kinetic models, including zero order, pseudo first order, Higushi, and Korsmeyer-Peppas models, were studied to understand the mechanism, and the results are demonstrated in **Figure 5.10(a)-(d)** for all the nanocomposites with TAE thermoset and **Figure 5.10(e)-(h)** for IO@CNF1.00/TAE at three different pHs.

The values of the rate constants (K), correlation coefficients (R^2) and release exponents (n) were reckoned as presented in **Table 5.4** for all IO@CNF/TAEs and TAE, while the parameters obtained for the kinetic study at three different pH media are tabulated in **Table 5.5**. From the R^2 values, it becomes clear that the release

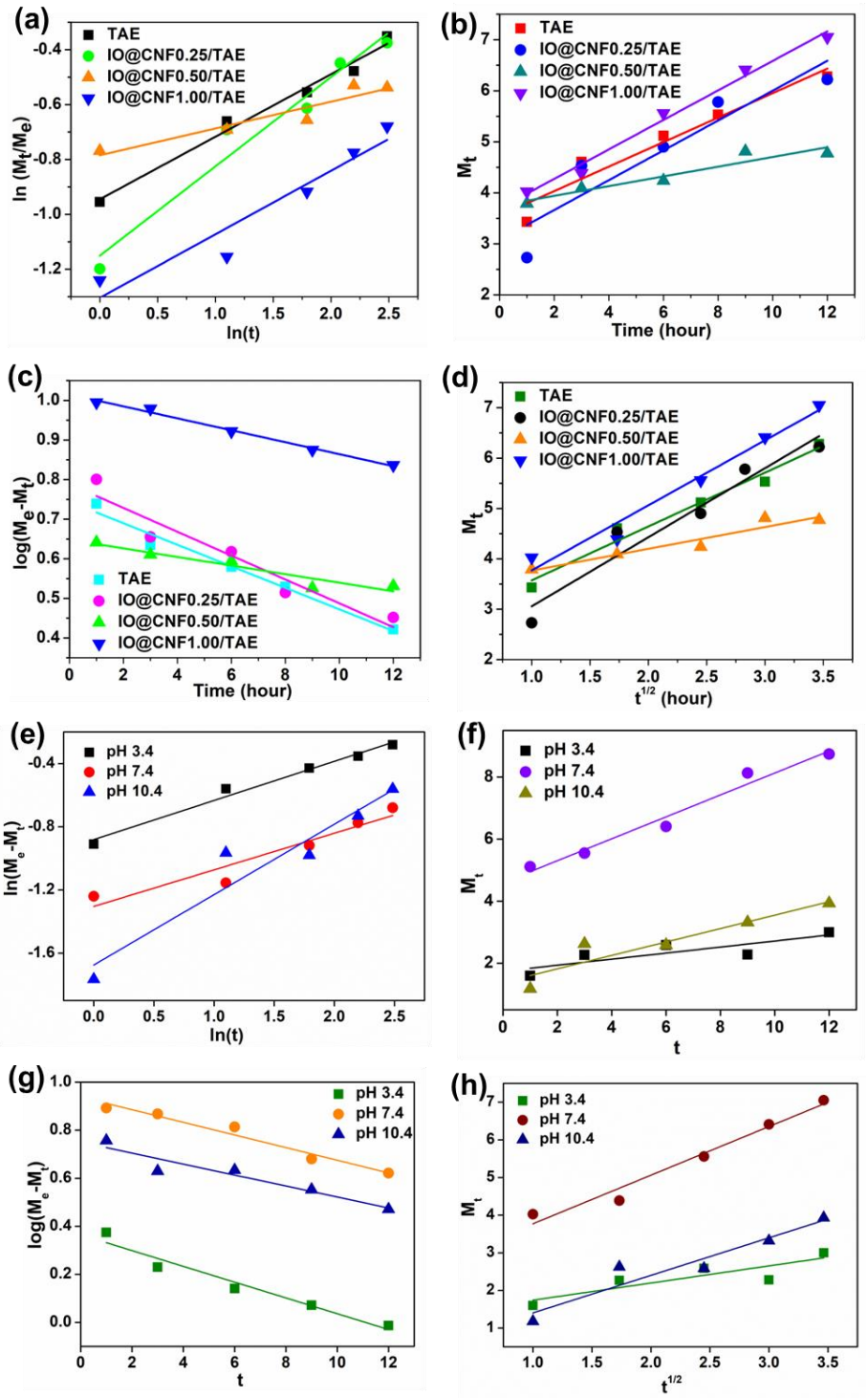

Figure 5.10: Kinetic data plots of AC release using (a) Korsmeyer-Peppas (b) zero order, (c) pseudo first order, and (d) Higushi models for the nanocomposite with TAE; and (e) Korsmeyer-Peppas, (f) zero order, (g) pseudo first order, (h) Higushi, models for IO@CNF1.00/TAE at three different pH environments

mechanism preferably followed the Higushi model, which is dominated by diffusion-controlled processes. The Higushi model was developed for water-soluble and low-soluble drugs incorporated inside semisolid or solid matrices [12]. However, when it comes to polymeric systems, this model fails to give accurate predictions, which can be achieved by using the Korsmeyer-Peppas model. The release exponent n values, as obtained from **Tables 5.4 and 5.5**, for the Korsmeyer-Peppas model, predicted the mechanism to be diffusion-driven. A n value of 0.5 or below indicates Fickian diffusion, while a n value from 0.5 to 1 signifies non-Fickian diffusion. In all the cases of the nanocomposites, the n values were lower than 0.5, which further confirmed a diffusion-controlled release of AC from the epoxy matrix. This occurred with the assistance of the nanohybrid, that permitted easy diffusion of the solvent medium into the matrix. The nanohybrids have hydrophilic CNFs and IONPs covered with polyphenolic groups with high water affinity. When the material was immersed in PBS, the medium slowly penetrated into the matrix, and the nanohybrid paved the way for the solvent to penetrate further and carry out the AC molecules attached to it. This seemed justified as increasing the content of the nanohybrid boosted the release rate.

Table 5.4: Kinetic parameters obtained from the kinetic study of the nanocomposites and TAE thermoset

Sample	Korsmeyer Peppas Power law			Zero order		Pseudo-first order		Higushi square root law	
	R^2	K_m	n	R^2	K_0	R^2	K_1	R^2	K_H
TAE	0.97	0.38	0.22	0.91	0.24	0.96	0.06	0.96	1.06
IO@CNF0.25/ TAE	0.94	0.31	0.32	0.81	0.29	0.89	0.069	0.91	1.37
IO@CNF0.50/ TAE	0.86	0.45	0.09	0.88	0.09	0.87	0.024	0.89	0.43
IO@CNF1.00/ TAE	0.82	0.27	0.21	0.96	0.35	0.95	0.033	0.90	1.55

5.3.8. Antibacterial study of the drug-loaded nanocomposite

In order to further validate the drug release ability of the prepared material, 10 wt%

drug-loaded thermosets were subject to an antibacterial study. Seven different bacterial strains were selected for the test and all the pure nanocomposite thermosets (without drug encapsulated) showed negative results, indicating the absence of any inherent antibacterial activity in them. Interestingly, when AC drug was loaded into the nanocomposites, significant antibacterial activity was detected for four bacterial strains, viz., *SA*, *SP*, *YE*, and *KP*; however, for the other three stains (*PA*, *BC*, and *YC*), negative results were recorded. **Table 5.6** shows the ZOI values as recorded drug-loaded nanocomposite thermosets, and the corresponding pictures captured during the test are presented in **Figure 5.11(a)-(d)** for pure thermosets and **Figure**

Table 5.5: Kinetic parameters obtained for IO@CNF1.00/TAE at three different pH environments

pH	Korsmeyer Peppas Power law			Zero order		Pseudo-first order		Higushi square root law	
	R^2	K_m	n	R^2	K_0	R^2	K_1	R^2	K_H
pH 3.4	0.97	0.41	0.24	0.61	0.097	0.93	0.07	0.68	0.45
pH 7.4	0.89	0.27	0.44	0.96	0.35	0.95	0.06	0.96	01.29
pH 10.4	0.89	0.18	0.23	0.82	0.21	0.87	0.05	0.88	0.99

5.11(e)-(h) for drug-loaded thermosets (1 to 4 sequentially denoting TAE, IO@CNF0.25/TAE, IO@CNF0.50/TAE, and IO@CNF1.00/TAE, respectively). From the figures, it can be conferred that AC was successfully released from the thermosets into the medium that perturbed the growth of the bacteria in the vicinity of the thermosets. Moreover, the ZOI values showed a visible dependence on the nanohybrid concentration, as the maximum inhibitory effect was observed for IO@CNF1.00/TAE followed by IO@CNF0.50/TAE and IO@CNF0.25/TAE. The best performance of the AC loaded thermosets was observed for *SA*, with a maximum ZOI of 30 mm for IO@CNF1.00/TAE. For the strain *ST*, only IO@CNF1.00/TAE showed activity with a ZOI of 12 mm, while others remained inactive. On the other side, pure epoxy, as expected, showed the lowest ZOI among all the thermosets for *SA*, with a ZOI of 12 mm, while zero activity was

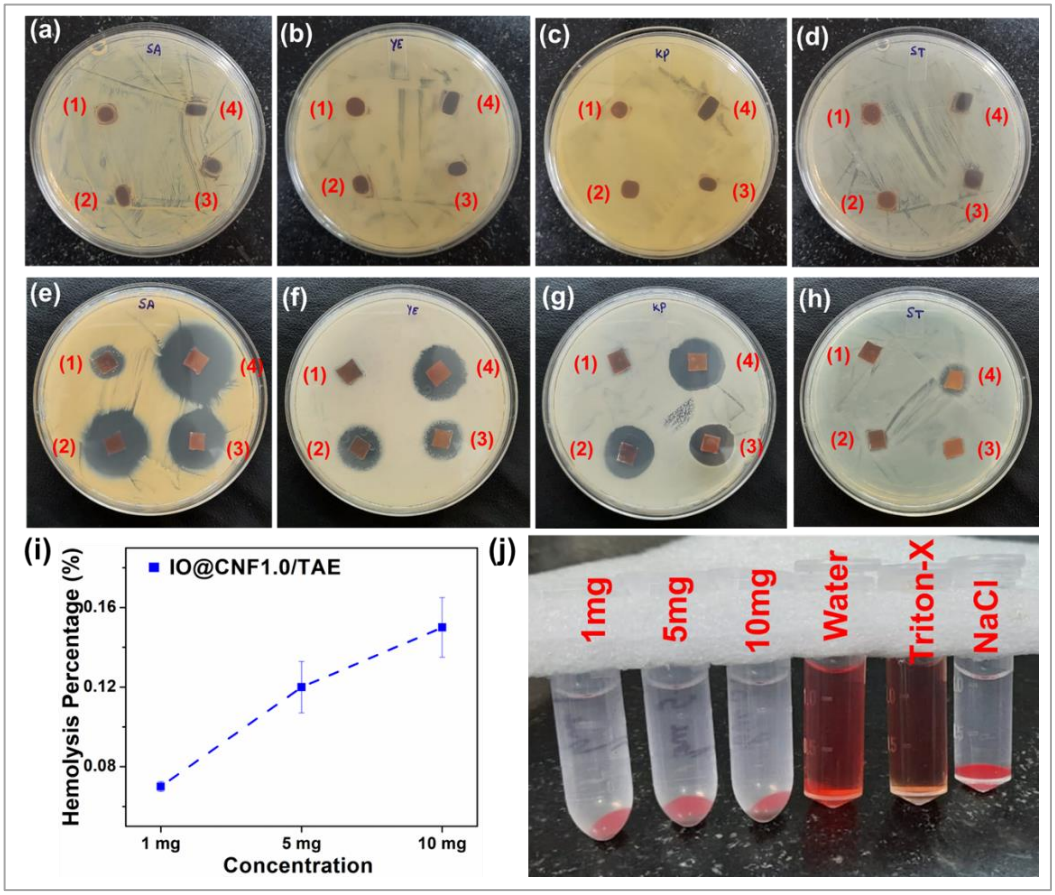

Figure 5.11: Antibacterial activity of pristine TAE (codded as 1) and nanocomposite (codded as 2, 3, and 4 for IO@CNF0.25/TAE, IO@CNF0.50/TAE, IO@CNF1.00/TAE, respectively) thermosets for (a) *SA*, (b) *YE*, (c) *KP*, and (d) *ST* strains (without drug) and drug encapsulated thermosets for (e) *SA*, (f) *YE*, (g) *KP*, and (h) *ST* strains; (i) concentration dependence behavior of hemolytic activity detected for IO@CNF1.00/TAE thermosets; and (j) specimens at different concentrations with positive and negative controls shown after completion of the test

detected for other strains. This clearly justifies the active role of the nanohybrid in releasing the drug molecules from the polymer network into the medium. The presence of the nanohybrid enables the diffusion of the media into the polymer network and carries the AC molecules out of the network.

5.3.9. Hemolysis study

The study of the impending hemolytic possibilities of a biomaterial is crucial to validate its applicability for blood-contacting applications. The presence of different functionalities on the surface of the biomaterial can facilitate the adhesion of blood platelets to the surface and activate blood coagulation and thrombosis [38]. The impending hemolysis study unveils the possibilities of the biomaterial triggering such effects when it comes into contact with blood. As per the ASTM F756

standard, the allowable hemolysis percentage of any biomaterial is below 5% [38]. A higher hemolysis percentage means potential toxicity as the red blood cells rupture when they come into contact with the material. Hence, the hemolysis test

Table 5.6: ZOI values of the antibacterial study obtained for the pure and drug loaded thermosets

Bacterial strain	ZOI (mm)			
	TAE	IO@CNF0.25/ TAE	IO@CNF0.50/ TAE	IO@CNF1.00/ TAE
SA	12	25	23	31
YE	0	17	15	21
KP	0	19	16	20
ST	0	0	0	12

was performed for the prepared nanocomposite with the highest nanohybrid content (i.e., 1.00 wt% for IO@CNF1.00/TAE) at three different concentrations (1 mg, 5 mg, and 10 mg). Fortunately, the prepared nanocomposite thermoset demonstrated excellent hemocompatibility that was found to be concentration-dependent. As shown in **Figure 5.11(i)**, the thermosets with 1 mg, 5 mg, and 10 mg concentrations exhibited very low hemolysis of 0.07%, 0.12%, and 0.15%. These values suggest unprecedently good biocompatibility of the nanocomposite compared to the positive controls, water (98.39%) and Triton-X (92.17%), where high hemolysis was observed, as apparent from **Figure 5.11(j)** showing the test samples after completion of the experiment. The epoxy/chitosan composite prepared by Soundhar et al. also revealed similar results with very low hemolysis percentages [39]. Thus, the findings of these studies indicated the absence of any toxic species on the surface of the nanocomposite thermosets or any leachate that can cause hemolysis, making it highly biocompatible, and thus the materials can be applied for blood-contacting applications.

5.3.10. *In vitro* biocompatibility study

The viability of the adherent HDF cells on the fabricated films and TCP were assessed using live-dead assay after 1 and 7 days of culture. After the seeding, the cells got attached to the surfaces of all the films, but they exhibited round morphology on day 1, as apparent from **Figure 5.12(b)-(e) (i)-(iii)**. In contrast, the cells grown over TCP exhibited normal spindle-shaped morphology with a spread cytoplasm (**Figure 5.12(a)**). On day 7, the cells were viable in all experimental and control groups. The cells grown on the TAE and IO@CNF1.00/TAE films showed mostly rounded morphologies and tended to grow in the form of aggregates as evident from **Figure 5.12(b) and (e) (iv)-(vi)**. However, the cells cultured on IO@CNF0.25/TAE and IO@CNF0.50/TAE films exhibited elongated spindle-shaped cellular morphology comparable to that of the TCP group as seen from the respective images (**Figure 5.12(c) and (d) (iv)-(vi))**. This suggests a favorable

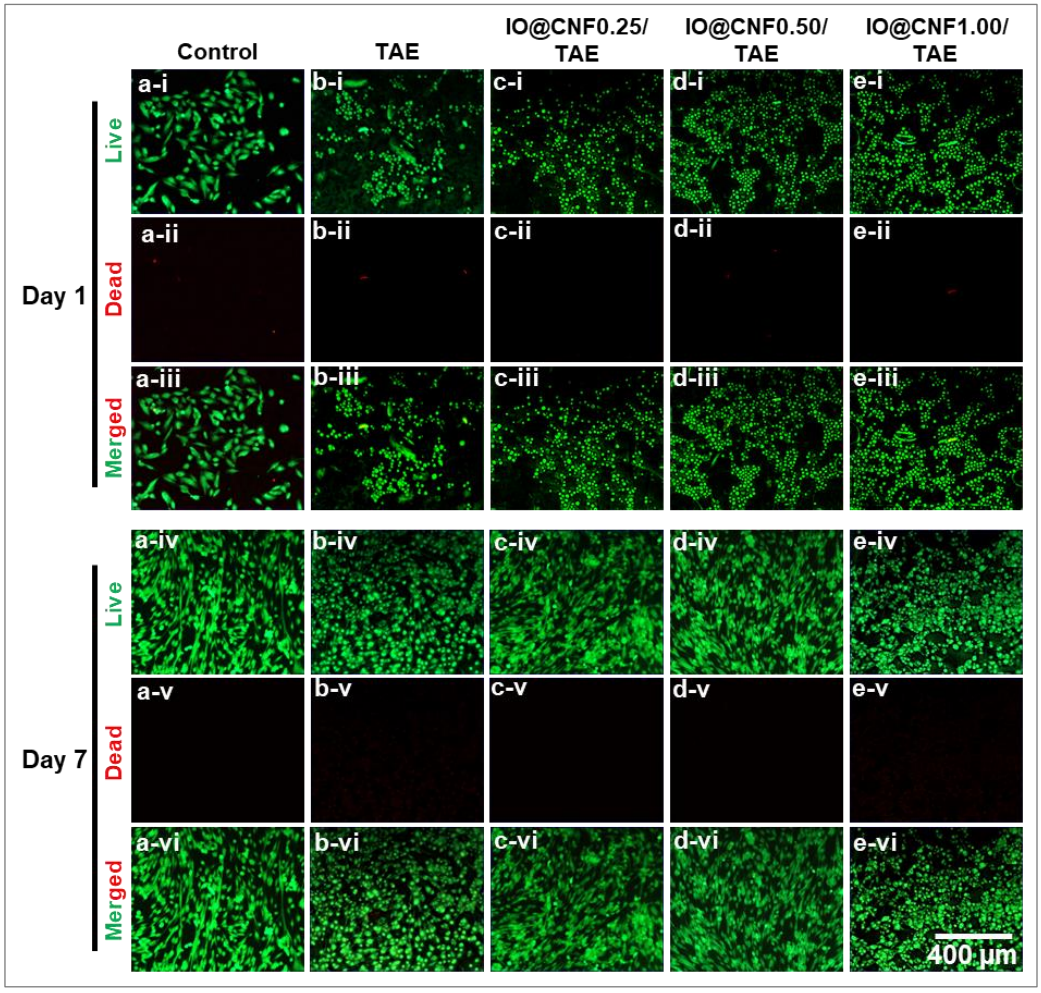

Figure 5.12: (a)-(e) Fluorescence micrographs showing cellular viability and morphology of HDF cells cultured on TCP control group and the fabricated films, TAE, IONP@CNF0.25/TAE, IONP@CNF0.50/TAE, and IONP@CNF1.00 /TAE, sequentially on day 1 and day 7 of post-seeding (scale bar: 400 µm)

concentration range of IONP@CNF for cellular growth to be 0.25 wt% to 0.50 wt%. Overall, the fabricated films did not show any cytotoxicity to HDF cells under in vitro condition, as cells remained viable and adhered when cultured on the films. These results efficiently depicted the non-toxic and bio-compatible nature of the prepared materials to be employed as drug carrying devices.

5.3.11. Biodegradation study

Assessing the biodegradability of a material is crucial for expanding its applicability in different realms. Specifically, to be practicable in the biomedical field, it becomes vital for the material to degrade automatically after its successful service life. To test the same, accelerated biodegradation was performed in the prepared nanocomposites without AC drug molecules triggered by the *BS* bacterial strain for a period of 30 days. During this time period, the growth of the bacterial solutions in the presence of the nanocomposites was monitored by measuring the OD of the bacterial solutions at regular intervals. As apparent from **Figure 5.13(a)**, bacterial growth gradually decreased in the presence of TAE thermosets. While, for the nanocomposites, the drop was visible in the bacterial growth but in a less intense way. The fact that the presence of the nanohybrid in the nanocomposites offered biocompatibility that helped the bacteria survive in the solution even in the presence of the nanocomposites. From the weight loss profiles as shown in **Figure 5.13(b)**, similar inferences can be drawn that the nanocomposites suffered greater weight loss compared to the TAE thermoset. A maximum weight loss of 11.01% was recorded for IO@CNF0.25/TAE followed by 10.15% for IO@CNF1.00/TAE and 9.95% for IO@CNF0.50/TAE. On the other side, the TAE thermoset exhibited a weight loss of only 8.19%. The SEM images of IO@CNF0.25/TAE thermoset recorded before and after biodegradation are displayed in **Figure.13(c)) and (e)-(f),** respectively. It is evident from the figures that the presence of the microbes triggered the degradation by gradually eroding and generating surface instabilities in the thermosets that were initially absent. The results obtained from the study revealed the good biodegradability of the prepared thermosets, enabling their application to various realms, with special emphasis given to biomedical applications.

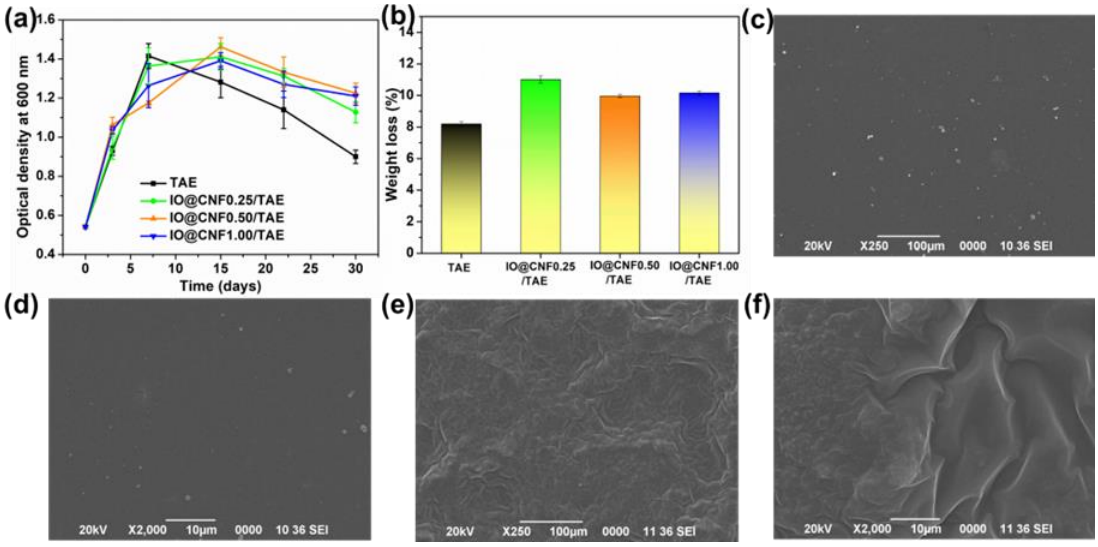

Figure 5.13: (a) Bacterial growth profiles, measured by OD at 600 nm, (b) weight loss percentage of the biodegraded nanocomposites, and SEM images of the thermoset IO@CNF0.25/TAE (c)-(d) before degradation and (e)-(f) after degradation at different magnifications

5.4. Conclusion

In conclusion, a robust, biocompatible, and biodegradable epoxy-IONP@CNF nanocomposite was explicitly fabricated by sustainably growing IONPs over the surface of CNFs and incorporating it in a bio-epoxy, TAE matrix. The facile growth of the nanoparticles was assisted by tea polyphenols exclusively extracted from WTFs, while the residual fibers were employed for the derivation of CNFs, which were used as the template for IONPs. The thermal and mechanical performances of the nanocomposites flaunted great improvements in comparison to the pristine epoxy, precisely with noteworthy enhancements in tensile strengths and T_gs. Additionally, on account of their biocompatibility and good performance, the nanocomposites can be envisaged for application in physiological environments to fulfill the crucial requirements of biomedical applications. To exemplify the same, nanocomposites were employed for the delivery of ampicillin, a potent antibiotic, under different pH conditions. The drug-releasing capability was further validated by exposing the drug-loaded nanocomposites to different bacterial environments, to exhibit their bactericidal activity. Thus, the strategy provided an effective means for designing epoxy-based nanocomposite systems as infection-resistant coatings for execution in implants or other devices of biomedical science.

References

[1] Valencia, L., Kumar, S., Nomena, E. M., Salazar-Alvarez, G., and Mathew, A. P. In-situ growth of metal oxide nanoparticles on cellulose nanofibrils for dye removal and antimicrobial applications. *ACS Applied Nano Materials*, 3(7):7172-7181, 2020.

[2] Lotfy, V. F. and Basta, A. H. Optimizing the chitosan-cellulose based drug delivery system for controlling the ciprofloxacin release versus organic/inorganic crosslinker, characterization and kinetic study. *International Journal of Biological Macromolecules*, 165:1496-1506, 2020.

[3] Motamedi, M., Ramezanzadeh, M., Ramezanzadeh, B., and Mahdavian, M. One-pot synthesis and construction of a high performance metal-organic structured nano pigment based on nanoceria decorated cerium (III)-imidazole network (NC/CIN) for effective epoxy composite coating anti-corrosion and thermo-mechanical properties improvement. *Chemical Engineering Journal*, 382:122820-122834, 2020.

[4] Sen, S., Singh, A., Kailasam, K., Bera, C., and Roy, S. Biomass-derived cellulose nanofibers and iron oxide-based nanohybrids for thermal insulation application. *Nanoscale Advances*, 4(16):3381-3390, 2022.

[5] Breijaert, T. C., Daniel, G., Hedlund, D., Svedlindh, P., Kessler, V. G., Granberg, H., Håkansson, K., and Seisenbaeva, G. A. Self-assembly of ferria–nanocellulose composite fibres. *Carbohydrate Polymers*, 291:119560, 2022.

[6] Ali, A., Zafar, H., Zia, M., ul Haq, I., Phull, A. R., Ali, J. S., and Hussain, A. Synthesis, characterization, applications, and challenges of iron oxide nanoparticles. *Nanotechnology, Science and Applications*, 9:49-67, 2016.

[7] Plachtová, P., Medrikova, Z., Zboril, R., Tucek, J., Varma, R. S., and Maršálek, B. Iron and iron oxide nanoparticles synthesized with green tea extract: Differences in ecotoxicological profile and ability to degrade malachite green. *ACS Sustainable Chemistry & Engineering*, 6(7):8679-8687, 2018.

[8] Zou, Y., Jin, X., Zhang, X., Kong, X., Zhang, Q., Xie, X., Liu, C., Ke, L., Liu, W., and Wang, W. A multifunctional biomedical patch based on hyperbranched epoxy polymer and MXene. *Science China Technological Sciences*, 64(12):2744-2754, 2021.

[9] Hassanzadeh, J., Al Lawati, H. A., and Al Lawati, I. Metal–organic framework loaded by rhodamine B as a novel chemiluminescence system for the paper-based analytical devices and its application for total phenolic content determination in food samples. *Analytical Chemistry*, 91(16):10631-10639, 2019.

[10] Rather, M. A., Deori, P. J., Gupta, K., Daimary, N., Deka, D., Qureshi, A., Dutta, T. K., Joardar, S. N., and Mandal, M. Ecofriendly phytofabrication of silver nanoparticles using aqueous extract of *Cuphea carthagenensis* and their antioxidant potential and antibacterial activity against clinically important human pathogens. *Chemosphere*, 300:134497, 2022.

[11] Bhar, B., Chakraborty, B., Nandi, S. K. and Mandal, B. B. Silk-based phyto-hydrogel formulation expedites key events of wound healing in full-thickness skin defect model. *International Journal of Biological Macromolecules*, 203:623-637, 2022.

[12] Chime, S. A., Onunkwo, G. C. and Onyishi, I. I. Kinetics and mechanisms of drug release from swellable and non swellable matrices: A review. *Research Journal of Pharmaceutical, Biological, and Chemical Sciences*, 4(2):97-103, 2013.

[13] Sarmah, D., Rather, M. A., Sarkar, A., Mandal, M., Sankaranarayanan, K., and Karak, N. Self-cross-linked starch/chitosan hydrogel as a biocompatible vehicle for controlled release of drug. *International Journal of Biological Macromolecules*, 237:124206, 2023.

[14] Yuan, Y., Ma, M., Zhang, S., and Wang, D. Efficient utilization of tea resources through encapsulation: Dual perspectives from core material to wall material. *Journal of Agricultural and Food Chemistry*, 71(3):1310-1324, 2023.

[15] Karavasilis, M. and Tsakiroglou, C. D. Synthesis of aqueous suspensions of zero-valent iron nanoparticles (nZVI) from plant extracts: Experimental study and numerical modeling. *Emerging Science Journal*, 3(6):344-360, 2019.

[16] Khatami, M., Alijani, H. Q., Fakheri, B., Mobasseri, M. M., Heydarpour, M., Farahani, Z. K., and Khan, A.U. Super-paramagnetic iron oxide nanoparticles (SPIONs): Greener synthesis using Stevia plant and evaluation of its antioxidant properties. *Journal of Cleaner Production*, 208:1171-1177, 2019.

[17] Rajendran, A., Alsawalha, M., and Alomayri, T. Biogenic synthesis of husked rice-shaped iron oxide nanoparticles using coconut pulp (*Cocos nucifera L.*) extract for photocatalytic degradation of Rhodamine B dye and their in vitro

antibacterial and anticancer activity. *Journal of Saudi Chemical Society*, 25(9):101307-101320, 2021.

[18] Bibi, I., Nazar, N., Ata, S., Sultan, M., Ali, A., Abbas, A., Jilani, K., Kamal, S., Sarim, F. M., Khan, M. I., and Jalal, F. Green synthesis of iron oxide nanoparticles using pomegranate seeds extract and photocatalytic activity evaluation for the degradation of textile dye. *Journal of Materials Research and Technology*, 8(6):6115-6124, 2019.

[19] Liu, S., Yao, K., Fu, L. H., and Ma, M. G. Selective synthesis of Fe_3O_4, γ-Fe_2O_3, and α-Fe_2O_3 using cellulose-based composites as precursors. *RSC Advances*, 6(3):2135-2140, 2016.

[20] Sebehanie, K. G., Legese, S. S., del Rosario, A. V., Ali, A. Y., and Olu, F. E. Facile preparation of magnetite–cellulose nanocomposite from a sustainable resource. *Bulletin of Materials Science*, 46(1):26-34, 2023.

[21] Dutta, G. K. and Karak, N. Waste brewed tea leaf derived cellulose nanofiber reinforced fully bio-based waterborne polyester nanocomposite as an environmentally benign material. *RSC Advances*, 9(36):20829-20840, 2019.

[22] Kargar, P. G., Noorian, M., Chamani, E., Bagherzade, G., and Kiani, Z. Synthesis, characterization and cytotoxicity evaluation of a novel magnetic nanocomposite with iron oxide deposited on cellulose nanofibers with nickel (Fe_3O_4@NFC@ONSM-Ni). *RSC Advances*, 11(28):17413-17430, 2021.

[23] Martínez-Cabanas, M., López-García, M., Barriada, J. L., Herrero, R., and de Vicente, M. E. S. Green synthesis of iron oxide nanoparticles. Development of magnetic hybrid materials for efficient As (V) removal. *Chemical Engineering Journal*, 301:83-91, 2016.

[24] Kouhbanani, M. A. J., Beheshtkhoo, N., Taghizadeh, S., Amani, A. M., and Alimardani, V. One-step green synthesis and characterization of iron oxide nanoparticles using aqueous leaf extract of *Teucrium polium* and their catalytic application in dye degradation. *Advances in Natural Sciences: Nanoscience and Nanotechnology*, 10(1):015007-015013, 2019.

[25] Bhuiyan, M. S. H., Miah, M. Y., Paul, S. C., Aka, T. D., Saha, O., Rahaman, M. M., Sharif, M. J. I., Habiba, O., and Ashaduzzaman, M. Green synthesis of iron oxide nanoparticle using *Carica papaya* leaf extract: Application for photocatalytic degradation of remazol yellow RR dye and antibacterial activity. *Heliyon*, 6(8):e04603-e04616 , 2020.

[26] Baghdadi, Y. N., Youssef, L., Bouhadir, K., Harb, M., Mustapha, S., Patra, D., and Tehrani-Bagha, A. R. Thermal and mechanical properties of epoxy resin reinforced with modified iron oxide nanoparticles. *Journal of Applied Polymer Science*, 138(23):50533-50547, 2021.

[27] Kim, H. C., Panicker, P. S., Kim, D., Adil, S., and Kim, J. High-strength cellulose nanofiber/graphene oxide hybrid filament made by continuous processing and its humidity monitoring. *Scientific Reports*, 11(1):13611-13623, 2021.

[28] Radu, T., Iacovita, C., Benea, D., and Turcu, R. X-ray photoelectron spectroscopic characterization of iron oxide nanoparticles. *Applied Surface Science*, 405:337-343, 2017.

[29] Yamashita, T. and Hayes, P. Analysis of XPS spectra of Fe^{2+} and Fe^{3+} ions in oxide materials. *Applied Surface Science*, 254(8):2441-2449, 2008.

[30] Kasote, D. M., Lee, J. H., Jayaprakasha, G. K. and Patil, B. S. Seed priming with iron oxide nanoparticles modulate antioxidant potential and defense-linked hormones in watermelon seedlings. *ACS Sustainable Chemistry & Engineering*, 7(5):5142-5151, 2019.

[31] Bhosale, M. A., Ummineni, D., Sasaki, T., Nishio-Hamane, D., and Bhanage, B. M. Magnetically separable γ-Fe_2O_3 nanoparticles: An efficient catalyst for acylation of alcohols, phenols, and amines using sonication energy under solvent free condition. *Journal of Molecular Catalysis A: Chemical*, 404:8-17, 2015.

[32] Xu, Z., Ye, H., Li, H., Xu, Y., Wang, C., Yin, J., and Zhu, H. Enhanced lithium ion storage performance of tannic acid in LiTFSI electrolyte. *ACS Omega*, 2(4):1273-1278, 2017.

[33] Cardillo, D., Sencadas, V., Devers, T., Islam, M. M., Tehei, M., Rosenfeld, A., Boutard, T., Rocher, E., Barker, P. J., and Konstantinov, K. Attenuation of UV absorption by poly (lactic acid)-iron oxide nanocomposite particles and their potential application in sunscreens. *Chemical Engineering Journal*, 405:126843-126851, 2021.

[34] Yue, L., Liu, F., Mekala, S., Patel, A., Gross, R. A., and Manas-Zloczower, I. High performance biobased epoxy nanocomposite reinforced with a bacterial cellulose nanofiber network. *ACS Sustainable Chemistry & Engineering*, 7(6):5986-5992, 2019.

[35] Jung, J. and Sodano, H. A. Cellulose nanocrystal functionalized aramid nanofiber reinforced epoxy nanocomposites with high strength and toughness. *Nanotechnology*, 34(24):245703-245717, 2023.

[36] Thipperudrappa, S., Ullal Kini, A., and Hiremath, A. Influence of zinc oxide nanoparticles on the mechanical and thermal responses of glass fiber-reinforced epoxy nanocomposites. *Polymer Composites*, 41(1):174-181, 2020.

[37] Aslan, A., Salur, E., Düzcükoğlu, H., Şahin, Ö. S., and Ekrem, M. The effects of harsh aging environments on the properties of neat and MWCNT reinforced epoxy resins. *Construction and Building Materials*, 272:121929-121949, 2021.

[38] Talebi, A., Labbaf, S., Atari, M., and Parhizkar, M. Polymeric nanocomposite structures based on functionalized graphene with tunable properties for nervous tissue replacement. *ACS Biomaterials Science & Engineering*, 7(9):4591-4601, 2021.

[39] Soundhar, A. and Jayakrishna, K. Investigations on mechanical and morphological characterization of chitosan reinforced polymer nanocomposites. *Materials Research Express*, 6(7):075301-075316, 2019.